State of the Surface of Antibacterial Copper in Phosphate Buffered Saline

Cigdem Toparli,[a] Stefan W. Hieke,[a] Abdulrahman Altin,[a] Olga Kasian,[a,*] Christina Scheu,[a] and Andreas Erbe[a,b,z]

[a]*Max-Planck-Institut für Eisenforschung GmbH, Department of Interface Chemistry and Surface Engineering, 40237 Düsseldorf, Germany*
[b]*Department of Materials Science and Engineering, NTNU, Norwegian University of Science and Technology, 7491 Trondheim, Norway*

The state was investigated of the copper surface in phosphate buffered saline (PBS; 140 mM Cl^-, 10 mM phosphate; pH 7) by a combination of cyclic voltammetry (CV) and chronoamperometry (CA) with in situ spectroscopic ellipsometry and Raman spectroscopy. After polarization, samples were analyzed ex situ. In agreement with expectations on the basis of the Pourbaix diagram, Cu_2O and Cu_4O_3 were observed when polarizing the system above ≈−0.05 V vs. Ag|AgCl|3M KCl. The formation of Cu_2O did not lead to a passivation of the system. Rather, the system dissolved under formation of soluble square planar $CuCl_4^{2-}$, identified by its strong Raman peak ≈300 cm^{-1}. During dissolution, spectroscopic ellipsometry showed a film with a stable steady state thickness. Energy electron loss spectroscopy (EELS) analysis of a cross section of the oxide after removal from the electrolyte showed that the oxide was Cu_2O. It is suggested that Cl^- replaces oxygen vacancies in the oxide layer. As soon as oxidation to Cu^{II} becomes dominant, the dissolution proceeds to soluble Cu^{II} species. The outer surface of copper under these conditions is hence a Cu_2O-like surface, with Cu^{II} complexes present in solution.

Manuscript submitted May 15, 2017; revised manuscript received July 18, 2017. Published August 9, 2017.

Copper is known for its antibacterial activity.[1–3] The importance has been pointed out of the physical chemistry of the copper/environment interface for the "contact killing" of bacteria by copper.[4] In contact with any electrolyte-containing medium, such as bacteria, copper may actively corrode, implying copper dissolution. Often, however, passivating films form on copper. Electrochemical reactions at the copper/electrolyte interface were extensively studied, because copper is one of the most important metals in the industry, because of its corrosion resistance, its good electrical and thermal conductivity, and mechanical properties.[5–11]

Biological environments often contain high concentrations of Cl^-. In vitro antibacterial tests are typically performed in buffers, which represent complex electrolytes from the point of view of corrosion. Copper ion release from the metal, and oxide film formation in biological test solution, are accepted to be the key for bacteria killing.[1,4,12,13] While a number of works are available addressing the surface film formation on copper in alkaline electrolytes,[14–17] much less physical-chemical data is available for conditions when active corrosion is possible,[18] and to our knowledge, the state of the surface during electrochemical polarization in a biochemical buffer has not been investigated. However, a number of reactions are possible in the typical biochemical buffers, in addition to those present in usual aqueous electrochemistry. One buffer frequently used in biochemical tests is phosphate buffered saline (PBS).[19] In PBS, corrosion products based on copper oxides and hydroxides, copper chloride, copper phosphates, or mixed phases may develop. The state of the copper surface shall be investigated in situ in this work, under controlled electrode potential, mimicking possible processes in contact with a solution containing microorganisms.

Film formation on copper during high temperature atmospheric oxidation yields a duplex oxide layer consisting of Cu_2O as inner layer and CuO as outer layer.[20–22] In a previous study, we showed that the formation of Cu_4O_3 occurs during the oxidation of Cu in alkaline environment.[17] The interactions of copper oxides with complexing ions such as Cl^- are rather complicated.[7,23–26] Consequences of such interaction may be a localized attack, with loss of the oxide film.[27–29] Previous experimental studies repetitively showed that the presence of Cl^- in the electrolyte leads to pitting corrosion, and thus instability of the oxide film, resulting in CuCl formation.[30]

A very early proposal for the corrosion mechanism of Cu in neutral Cl^--containing media assumed that the initial corrosion product is cuprous chloride, CuCl, which transformed into cuprous oxide, Cu_2O.[30] In later works, copper oxide formation in Cl^--containing media was suggested to be a precipitation reaction rather that an electrochemical process.[31,32] It was also suggested that the stability of Cu_2O depends on the concentration of chloride ions. On the other hand, some works showed that cupric oxide, CuO, or cupric hydroxide, $Cu(OH)_2$, could be detected as a function of surface preparation and electrolyte.[30,32–34] Overall, there is a lack of in situ investigations about formation of surface films in Cl^--containing media.

The film formation at the copper|electrolyte interface in general has been characterized by coupling electrochemical experiments to in situ characterization methods.[15–17] In situ Raman spectroscopy studies showed the potential dependent oxide formation.[18,35] Using their vibrational fingerprints in Raman spectroscopy, three main oxide phases of Cu can be easily identified.[36,37] Formation of CuCl and Cu_2O as function of electrode potential in Cl^--containing electrolyte was confirmed by surface enhanced Raman spectroscopy.[18] In situ scanning tunneling microscopy (STM) showed that the presence of Cl^- lead to an enhanced dissolution of Cu.[15,38,39]

In the present work, the electrochemical properties of copper in PBS were investigated. The state of the surface during cyclic voltammetry (CV) and chronoamperometry (CA) experiments was probed in situ and operando by spectroscopic ellipsometry (SE) and Raman spectroscopy. After electrochemical experiments, the internal structure of the formed corrosion product layers was analyzed ex situ by scanning electron microscopy (SEM), transmission electron microscopy (TEM), electron energy loss spectroscopy (EELS), and X-ray photoelectron spectroscopy (XPS).

Experimental

Sample preparation.—Evaporated Cu was used as working electrode both for in situ SE and in situ Raman spectroscopy during CV experiments. For CA experiments, polycrystalline Cu foil was used to avoid the detection of the strong fundamental Si phonon in Raman spectra, which might or might not be observed due to the high total amount of copper dissolution.

For evaporated samples, Si(100) wafers (Siegert Wafer) were used as substrates. The wafers were cleaned with neutral detergent (Extran; VWR), rinsed with deionized water, 2-propanol, and then dried.

*Electrochemical Society Member.
[z]E-mail: copper-in-pbs@the-passivists.org

Chromium and copper pellets with purity 99.999% (Wieland Edelmetalle) were used for electron beam evaporation. All evaporation was carried out in a Leybold Univex 450 chamber. The base vacuum before the evaporation was around $6 \cdot 10^{-7}$ mbar. Firstly, a 10 nm chromium adhesion layer was deposited. Subsequently, copper was evaporated at an evaporation rate of 10 nm min^{-1}. Layers of 200 nm overall thickness were prepared.

Polycrystalline Cu foils with a purity of 99.5% (Goodfellow) were mechanically ground with SiC paper up to 4000 grit, and subsequently polished with different polishing suspension (3 μm and 1 μm diameter SiO_2, pH = 9) to obtain a smooth surface. Samples were subsequently rinsed with ethanol, and sonicated in ethanol for 5 min to remove residual polishing suspension, before being dried in a nitrogen stream.

In situ SE.—In situ SE experiments were performed using an optical-electrochemical cell. The details of the in situ cell were described elsewhere.[40,41] The copper surfaces served as working electrodes in the experiments. Copper tape was used to provide the electrical contact of the surface of the sample. A Pt mesh counter electrode and Ag|AgCl|3M KCl microreference electrode (DriRef-2SH, World Precision Instruments) were used to measure current flow and to control the electrode potential, respectively. The electrode potential of the microreference electrode was determined as +0.208 mV vs. standard hydrogen electrode by a calibrated Ag|AgCl|3M KCl electrode (Metrohm). All electrode potentials reported in this work are referenced against Ag|AgCl|3M KCl. Phosphate-buffered saline (PBS, 140 mM NaCl, 10 mM total phosphate, pH 7), was used as electrolyte. The electrolyte was externally purged with argon, and flown through the cell with a rate of 2 mL min^{-1} using a peristaltic pump (Ismatec IDEX Health and Science). During the measurement, the pump rate was reduced to 10.6 μL min^{-1}. In this work, duration of a single ellipsometric measurement was 23.5 s.

The cell was placed under a spectroscopic ellipsometer SE 800 (Sentech Instruments), working in the wavelength range of 280-810 nm (1.5-4.4 eV). A Compactstat potentiostat (Ivium Technologies) was used to control potentials and measure currents.

Raman spectroscopy.—In situ Raman spectra were obtained using a Labram confocal Raman microscope (Horiba). An objective with magnification 10×, numerical aperture 0.25, was used to illuminate the sample with light from the 632 nm (1.96 eV) line of a HeNe laser. A home-built Teflon cell was used.[42] A graphite rod was used as a counter electrode, while the same microreference electrode as during in situ SE experiments was used. Each spectrum was acquired for 30 s.

For ex situ experiments, in addition to the 632 nm laser, light from the 514 nm (2.41 eV) line of an Ar^+ laser was also used.

XPS.—XPS measurements were performed (Quantera II, Physical Electronics) applying a monochromatic Al Kα X-ray source (1486.6 eV) operating at 15 kV and 25 W. The binding energy scale was referenced to the C 1s signal at 285.0 eV. For investigation of the change of elemental composition with depth, sputtering with Ar plasma has been carried out. Sputtering time of 1 min corresponded to the removal of approximately 3 nm of Cu. These sputtering rates were calculated from the depth profiles of the Cu samples with defined thickness. The sputtering spot size was 2 mm × 2 mm. Analysis of the spectra has been carried out with the Casa XPS software (http://www.casaxps.com/). In addition to research articles, the Lasurface database (http://www.lasurface.com) was used to aid interpretation.

Electron microscopy and EELS.—Microstructural characterization was carried out by SEM and TEM. The microstructure of the samples were investigated with back scattered electron (BSE) imaging in a dual-beam Zeiss 1540XB scanning electron microscope (SEM) equipped with a Edax Apollo XL EDX camera. Top view micrographs were taken by SEM (JEOL JSM-6450). Cross-sectional specimens were prepared in a dual beam focused-ion-beam system (600i dual beam SEM/FIB) using the lift out technique,[43] in a modification of a procedure described elsewhere.[44,45] TEM investigations were performed in a probe-corrected FEI Titan Themis 60-300 X-FEG S/TEM instrument equipped with a FEI Super-X windowless energy-dispersive X-ray spectroscopy (EDX) system with four synchronized silicon drift detectors and a post column Gatan GIF Quantum ERS energy filter.

The instrument was operated at 300 kV in scanning TEM (STEM) mode with a spot size of about 1.5 Å. For STEM imaging, a probe current of ≈80 pA was used, while EDX measurements were performed with 400 pA, and EELS measurements with 80 and 320 pA. STEM images were recorded with a convergence semi-angle of 23.8 mrad using a Fischione Instruments Model 3000 high angle annular dark-field (HAADF) detector with inner and outer collection semi-angles of 73 and 352 mrad, respectively.

For electron energy loss near-edge structure (ELNES) analysis of the O K edge (edge onset at ≈532 eV),[46,47] and the Cu $L_{2/3}$ edge (onset at ≈931 eV)[46,47] spectra with a dispersion of 0.25 eV/channel and an entrance aperture of 2.5 mm were recorded in dual EELS mode,[48] at a collection angle of 35 mrad. The full width at half maximum (FWHM) of the zero loss was 0.9 eV. 20 spectra were taken at an acquisition time of 1.0 s and summed up to obtain high signal to noise ratios. All spectra were corrected for the dark current and channel-to-channel gain variation. The pre-edge background was extrapolated using a power law function and subtracted from the original spectrum.[47] The edge onset was measured at the FWHM of the first onset. The thickness of the different layers was determined by analysis of 6 different regions of interest and is stated as mean ± standard deviation. In addition, the minimum to maximum value is given.

Thermodynamic analysis.—Potential-pH predominance diagrams were calculated using the freely available program MEDUSA (http://www.kth.se/en/che/medusa/chemeq-1.369367; https://sourceforge.net/projects/eq-diagr/) and its standard HYDRA database. MEDUSA calculates equilibrium predominance diagrams of complex systems. In total 59 soluble and 9 insoluble compounds were considered, containing Cu, P, Cl, O and H in all relevant oxidation states. All calculations were carried out for a temperature of 25°C, close to the experimental temperature, and the temperature used in the HYDRA data basis. No correction for activity coefficients was used.

Results and Discussion

In situ characterization of surfaces during potentiodynamic polarization.—A CV and the corresponding thickness d of the growing layer of oxidation products is shown in Fig. 1. The layer thickness was obtained using ellipsometric data based on the analysis of the shift in ellipsometric parameter Δ,[17] with a calibration reported previously.[12]

The CV of copper in PBS is different from those obtained in alkaline electrolyte.[14,15,18,49,50] The CV in the potential region from −1.0 V to 0.1 V exhibited two reduction peaks (C_1 and C_2) and one accompanying anodic feature (A_1). The initially observed cathodic features are attributed to the reduction of initially present surface oxide. The related anodic peak (A_1) is in alkaline electrolyte typically associated with oxidation of copper to Cu_2O.[14,15,18,49,50] The current density increased continuously after the electrode potential reached ≈−0.1 V, indicating a high metal dissolution rate. A more detailed CV peak assignment was obtained by in situ Raman spectroscopy, and will be discussed later in this section.

Initially, the layer thickness increased from 1.5 nm to 7 nm after starting to apply a controlled potential. During the cathodic scan, the layer thickness decreased and the layer essentially disappeared because of reduction. In the anodic scan, the first increase in layer thickness was observed when the potential reached ≈0 V. Subsequently, the layer thickness increased up to ≈15 nm, simultaneously with the increase in the current density.

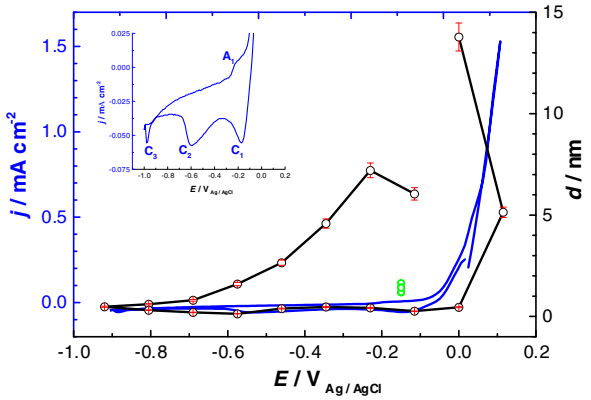

Figure 1. First ellipsometric CV scan (—) in PBS (started 0 V, first in negative direction). The current density j and thickness d (○) are plotted against electrode potential E. The scan rate was 5 mV s^{-1}, thus each SE spectrum averages over 120 mV. The first 3 SE measurements (○) were recorded at open circuit potential (OCP, ≈−150 mV). Inset: Same CV as in main graph with smaller current range, clearly showing the redox peaks.

In order to determine the nature of the layer on Cu in PBS solution, in situ Raman spectroscopy experiments were performed. The neutral pH buffered system is interesting to investigate under these condition, because thermodynamically, in the presence of Cl^- the formation of the Cu_2O and CuCl films are possible.[18,51] In the presence of

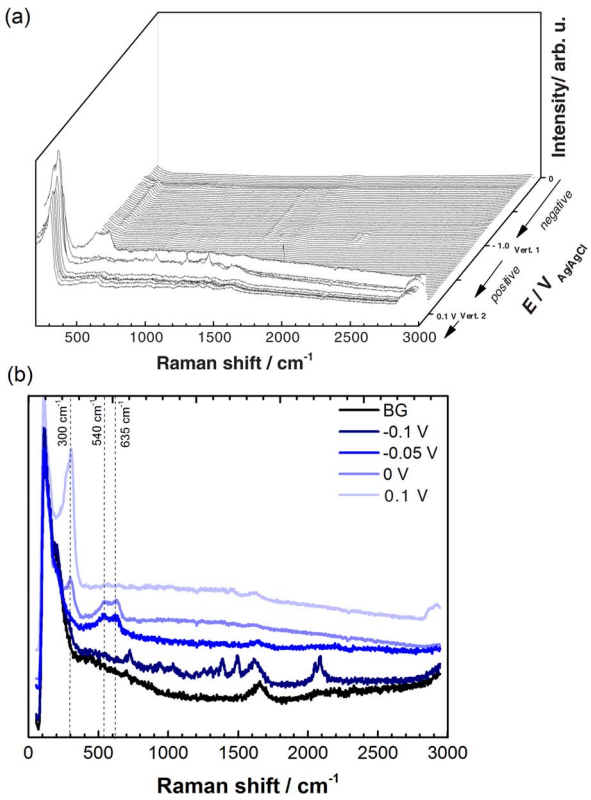

Figure 2. (a) Evolution of in situ Raman spectra collected during a CV with scan rate 5 mV s^{-1} in the potential range of −1.0 V and +0.1 V in PBS. Experiments proceeded from 0 V toward the negative vertex potential (Vert. 1) at −1.0 V, and the positive vertex potential (Vert. 2) at 0.1 V back to 0 V. (b) Examples of in situ Raman spectra collected during a CV at the potentials indicated in the graph. BG indicates an initial measurement at OCP. All other measurements were collected during the positive scan.

Table I. Raman peaks observed in this work with possible assignments to chemical species on the basis of literature assignments.[18,35–37,52,60,69] Reported peak wavenumbers of some oxides in the literature vary considerably.

System	In this work peak / cm^{-1}	Lit. peak / cm^{-1}	Ref.
$Cu^{II}O$	280	290	35–37
$Cu^{II}Cl_4^{2-}$	300	290	60
$Cu_2^{I}O$	400	400–490	18,36,37
$Cu_2^{I}Cu_2^{II}O_3$	530–560	540	36,37
$Cu^{II}O$	620	630–634	18,35,36
$Cu_2^{I}Cu_2^{II}O_3$	620	630	36,37
$Cu_2^{I}O$	620	635	18,35,36
$Cu_2^{II}(OH)_3Cl$	940	942	52,69
phosphates	1000–1100	1019	52,69
phosphates	1000–1100	1100	52,69

phosphate, precipitation of copper phosphates is a further possibility. Raman spectra recorded during CV are shown in Fig. 2.

The CV obtained during in situ Raman spectroscopy closely follows the CV in in situ SE. The main feature of aqueous phosphate oxyanions are two peaks at ≈930 cm^{-1} and ≈1000 cm^{-1},[52] which were not observed in this work. Control experiments with the pure electrolyte and the same illumination geometry as used for in situ experiments did not yield any phosphate peaks from the electrolyte itself. Discussion of the surface features shall concentrate on the positive scan in the CV. Here, anodic currents start to be observed at potentials above ≈-150 mV. From above ≈-50 mV, two Raman features at ≈540 and 635 cm^{-1} developed in the spectrum (Fig. 2), indicating the concurrent formation of Cu_2O and possibly Cu_4O_3, i.e. copper oxide species (Table I). At ≈0 V, a peak at slightly below 300 cm^{-1} started to develop. This peak dominated the spectra above ≈0.05 V, when the oxide peaks disappeared. The high intensity of the peak at ≈300 cm^{-1} suggests that it does not originate from adsorbed species. The assignment of this peak shall be discussed in the following.

In comparable works in NaOH,[17,53] no peak at ≈300 cm^{-1} was observed. Phosphate peaks around 1000 cm^{-1} are were not observed in the presence of this peak. Therefore, this peak must originate from a chloride-related species. On a similar line of reasoning, this peak was previously assigned to originate from "a Cu-Cl stretching mode of adsorbed chloride or copper chloride phase film".[18] Indeed, a number of works report Cu-Cl stretching modes at ≈290 cm^{-1}.[54–56] However, solid CuCl has no characteristic Raman feature in this region; rather, all strong Raman modes from CuCl are observed at lower wavenumbers.[57–59] Furthermore, the electrochemical data shows a continuing high dissolution rate, without even slight drops in current density. The species to which this mode belongs can therefore not inhibit the dissolution of copper. If a solid precipitate was forming, stochastic dips in current density would be expected, which were not observed here. Neither were they observed in CA experiments discussed below. On the other hand, a strong Raman feature at 286 cm^{-1} is characteristic for square planar $Cu^{II}Cl_4^{2-}$.[60] The occurrence of a Cu^{II} species is expected at higher electrode potentials, where the peak in question is observed. The high intensity of the peak is consistent with the presence of a large concentration of dissolved species in the near-interface region. Alternatively, the species may form directly at the interface, e.g. via adsorbed Cl^- as precursor. The interpretation is also consistent with the electrochemical data. Therefore, the peak at ≈300 cm^{-1} is assigned here to a Cu-Cl stretching mode of dissolved, adsorbed, or oxide-film incorporated $Cu^{II}Cl_4^{2-}$. Table I presents an overview of the vibrational modes of copper oxides and relevant other species observed in this work and a comparison with literature data.

The SE data was analyzed to obtain the absorption spectrum of the forming thin films (Fig. 3), to have additional information on the films. The electronic absorption spectrum of the oxide film on Cu formed in alkaline media was discussed in previous studies.[17,53] The

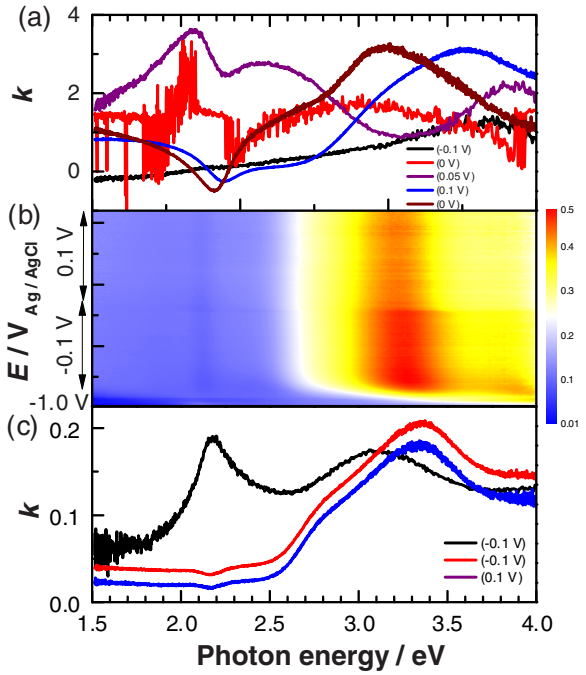

Figure 3. Imaginary part k of complex refractive index of the layers forming on copper obtained in situ (a) during the positive scan in a CV experiment in the potential range from −1.0 V to 0.1 V. Spectra are shown acquired during positive potential scan at −0.1 V (—), 0 V (—) and 0.05 V (—), at the positive vertex potential 0.1 V (—), and the final potential 0 V (—). (b) Color-coded k of the layer depending on electrode potential and time during a CA experiment. Color scale is given next to the graph. (c) Representative imaginary part k of refractive index of the layer in the potential range in the potential range of −1.0 V and 0.1 V, during a CA experiment.

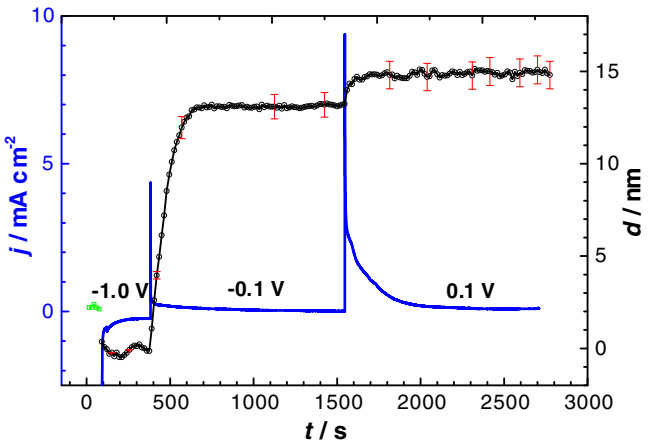

Figure 4. Current density j (—) and layer thickness d (○) as a function of time t of Cu in PBS during CA experiments at certain applied electrode potentials as indicated in the graph. The first 5 SE measurements (○) were recorded at OCP (≈−150 mV). Representative uncertainty estimates are shown on selected points only to keep the graph legible.

shape of the spectra obtained in PBS (Fig. 3) is qualitatively different from the ones obtained in alkaline environment.[17,53]

Fig. 3a shows absorption spectra obtained during a CV experiment. These spectra were obtained by an analysis procedure described in detail elsewhere.[17] Note, that thinner layers make the resulting spectra more sensitive to noise in the raw data. There were significant differences in the spectra depending on the electrode potential. When the potential reaches ≈0 V, peaks at ≈2.8 eV and ≈3.5 eV appeared, which are assigned to Cu_2O.[37] The strongest feature from CuCl is expected to be observed at 3.1 eV,[61] which may initially be hidden in the broad peak at 2.8 eV. The shape of the spectrum changed significantly with increasing potential. At 0.05 V, a feature at 2.1 eV dominated the spectrum. This feature has been interpreted as the "yellow" electronic absorption of Cu_2O, which is the forbidden direct band to band transition.[17] Activity in electrochemically formed films was attributed to the prevalence of defects.[17] The absorption spectrum acquired at 0.1 V (Fig. 3a) shows a minor peak at 2.3 eV and a broad feature at 3.4 eV. The peak at 2.3 eV indicates the presence of Cu_4O_3.[37] Assigning the broad feature at 3.4 eV unambiguously is not possible, because this peak might contain several components. The strongest electronic absorption feature from CuO is at 3.46 eV,[37] which agrees well with the observed feature. On the other hand, this broad peak has a shoulder at 3 eV which could originate from CuCl, which has a strong feature at 3.1 eV.[61] A feature around this region dominated the spectra in the later stages of the experiment. Summarising, the electronic absorption spectra agree with the Raman results as they point to an initial formation of oxides. At higher potentials, chlorides may be present in the film. In this whole discussion, the fact was neglected that roughening or lateral structuring of the surface will affect the conducted analysis, so that the obtained spectra should only be interpreted qualitatively.

In situ characterization of surfaces during potentiostatic polarization.—In CA experiments, preformed oxides were initially reduced. In SE experiments, after 5 SE measurements at OCP, the preformed oxide of 2 nm thickness was reduced at −1.0 V for 5 min. The surface was subsequently oxidized at −0.1 V and 0.1 V for 20 min each as shown in Fig. 4. After a potential jump to −0.1 V, the current density stabilized at 0.05 mA cm^{-2} within 100 s. On the other hand, the thickness of the layer continuously increased during the first 350 s, before reaching a steady state value of 13 nm. When the potential was switched to 0.1 V, the typical spike in the current density was observed. Simultaneously the thickness of the layer increased and stabilized at 15 nm after 100 s.

Fig. 5 shows Raman spectra recorded during a CA experiment on Cu foil. As in CV experiments, during the reduction of the surface (Fig. 5a), no obvious changes were observed. The Raman spectrum at this stage showed mainly the water deformation mode at 1635 cm^{-1}. When the potential jumped to anodic conditions (Fig. 5b and 5c), the spectrum showed peaks in the range of 500-700 cm^{-1}, and also at 300 cm^{-1} (Fig. 5c).

After stepping the potential to −0.1 V, three main features became visible in the spectra in Fig. 5b,5c. The peaks at 530 cm^{-1} and 625 cm^{-1} indicate the oxidation of Cu to Cu_4O_3 and Cu_2O, respectively. The feature at 300 cm^{-1} may be assigned to presence of $Cu^{II}Cl_4^{2-}$, as discussed above. A significant change related to the potential jump from −0.1 to 0.1 V is the spectral shift of the latter peak from 300 cm^{-1} to 290 cm^{-1}. This observation suggests a transformation of the species from which the peak originated from. A shift due to effects of the changing electric field is unlikely, as no such shift was observed in CV experiments. Here, this shift is interpreted as a transformation of the ratio of CuO and $Cu^{II}Cl_4^{2-}$ contributing to the peak.

From the electronic absorption spectra shown in Fig. 3(b,c), it is obvious that the spectra acquired during CA are quite different from the spectra acquired during CV. The absorption spectra of the films recorded during CA experiments (Fig. 3b) shows the main absorption at 3.3 eV, which is assigned to Cu_2O.[37] Moreover, it is obvious that only minor changes occurred during the potential jump, confirming the slow growth of the film. Therefore, it is useful to compare spectra recorded at the very beginning of polarization at −0.1 V, and the last spectra recorded at 0.1 V (Fig. 3c). The very first spectrum has two peaks at 2.1 eV and 3.1 eV, assigned to the presence of both Cu_2O and CuCl.[37,61] As the current reached steady state, the feature at 2.1 eV disappeared, and the peak at 3.1 eV shifted to 3.3 eV. The

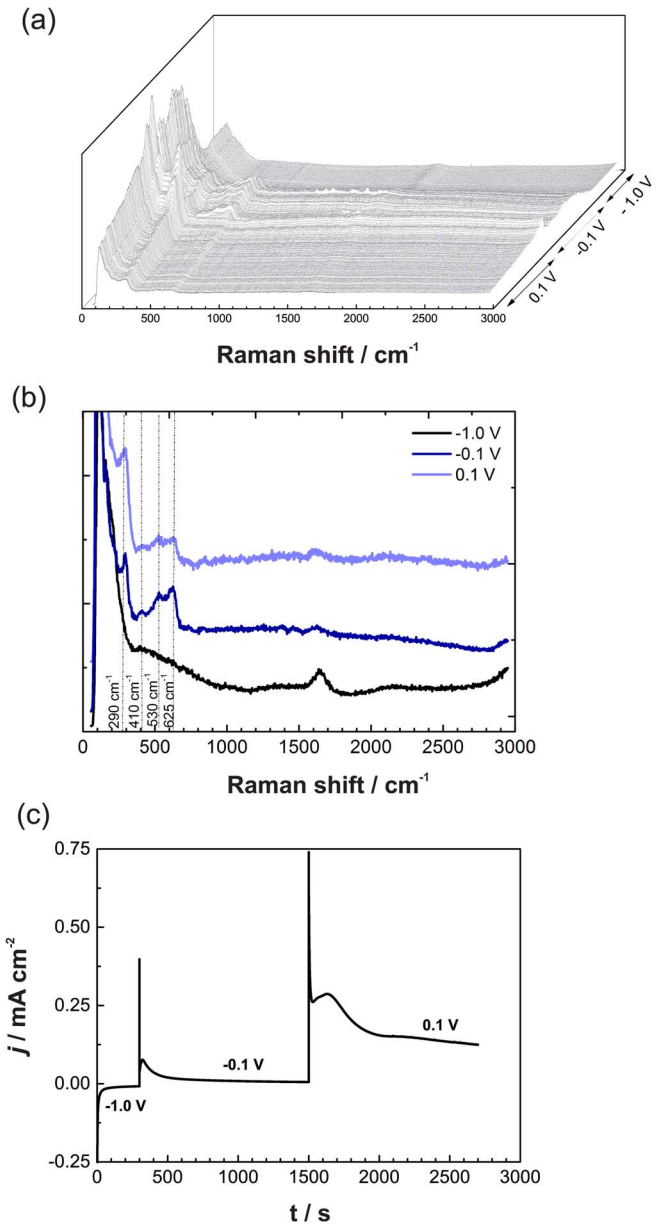

Figure 5. Evolution of in situ Raman spectra in CA experiments on a Cu foil. (a) full set of spectra in the potential range of −1.0 V to +0.1 V; (b) Spectra during the final stage of polarization at the three potentials chosen for this experiment; (c) CA data.

latter indicates an electronic transition from Cu_2O, complementing the Raman spectra (Fig. 5).

Surface characterization after electrochemical experiments.— Different samples were characterized with different ex situ methods after experiments. In this section, the focus is on samples after CA experiments. Top view SEM images of representative parts of the surface after in situ Raman CA experiments are shown in Fig. 6. Large parts of the surface were covered with needle shaped crystals. In certain regions, spherical features with an inner structure were observed. It is not immediately obvious whether these structures formed during the electrochemical treatment, or during removal of the samples from the electrolyte.

A sample after CA experiments was analyzed in more detail by STEM and EELS. Fig. 7 shows a STEM HAADF image and EDX elemental maps of the layer on top of the copper film. A continuous oxide film with a thickness of (38±10) nm (27–62 nm) was observed

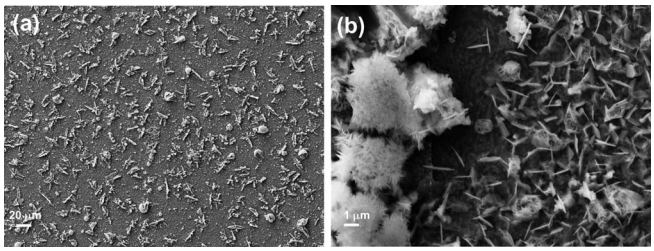

Figure 6. SEM images with two different magnifications of a copper surface after the full Raman CA experiment as shown in Fig. 5; (a) overview image, (b) magnified region showing the observed structures.

in the cross-sectional STEM HAADF micrographs. This thickness is higher than observed in situ by SE in the initial stages of the experiments, indicating significant oxide formation at OCP after switching off potential control, and during the removal of the sample from electrolyte and drying. In some regions, the oxide intruded into the Cu film as indicated by the arrow in the O EDX map. Different intrusion distances have been observed. In many cases, they are only a few nm at the former Cu surface. In a specific case shown in Fig. 7, intrusions range ≈70 nm into the copper. In some cases, intrusions over the full thickness of the copper film were observed, ranging up to the former Cr/Cu interface. The intrusion of the oxide layer could originate from pitting, induced by Cl^- ions, and subsequent repassivation of pits. The results make it clear that the oxide film is laterally inhomogeneous, at least at the end of the experiments. Additional oxide, likely a result of precipitation, was observed on top of the closed layer.

Several voids are visible in Fig. 7. Pores formed at the Cu/oxide [diameter (50 ± 17) nm, 26-81 nm] as well as at the Cr/Cu interface. EDX maps show an enrichment of Cl at the Cu/Cr interface. The high concentration of O depicted at the Cu/Cr interface is an artifact due to the overlap of the O K_α and Cr L lines. Nevertheless, the results indicate Cl^- diffusion through the film due to pitting and preferentially at the grain boundaries.

EELS measurements were acquired in STEM mode for different regions of the metallic Cu thin film including the surface layers. In Fig. 8, exemplary ELNES spectra of the Cu $L_{2/3}$ and the O K edge are shown for the various regions. No white lines were observed in the Cu $L_{2/3}$ ELNES of the Cu thin film, in accordance with literature spectra of metallic Cu, because of its fully occupied 3d band.[62,63] For the oxidized layer and the oxide feature on the top, white lines appear due to the partial emptying of the Cu 3d band.[62,63] No chemical shift was found for the Cu L_3 edge (edge onset ≈933 eV) of the oxide, indicating the presence of Cu^I.[64] No evidence was found for the presence of Cu^{II}, where an energy shift of ≈−2 eV with respect to metallic Cu is expected.[62] The presence of Cu^I is further confirmed by the white line intensity of the Cu L_3 edge, which should be much more pronounced for Cu^{II}.[64] The O K ELNES of both, the oxide layer and the feature on top, shows a sharp peak with an edge onset of 530 eV, followed by a broad peak at an energy loss of about 541 eV. A similar ELNES was reported in literature for Cu_2O.[62,64] No oxygen was found in the metallic Cu thin film.

In summary, the presence of Cu^I was confirmed by its ELNES fingerprint using the Cu $L_{2/3}$ as well as the O K edge. Moreover, no evidence for the existences of Cu^{II}, either in CuO or in Cu_4O_3 was observed by the ex situ EELS investigations of the specimen after electrochemical treatment and removal from the electrolyte. The existence of a Cu^I containing monolayer was reported for atomically sharp Cu| α-Al_2O_3 interfaces.[62] Surface roughness in the present work prevented a sharp interface in projection in TEM, thus the presence of a sub-nanometer layer containing Cu^{II} cannot be ruled out. Cu^{II} may also be present as minor component homogeneously distributed in the oxide layer below the EELS detection limit of ≈1%.[47] Alternatively, Cu^{II}-containing species might be present only when the surface is in contact with the aqueous solution. In general, for thin electro-

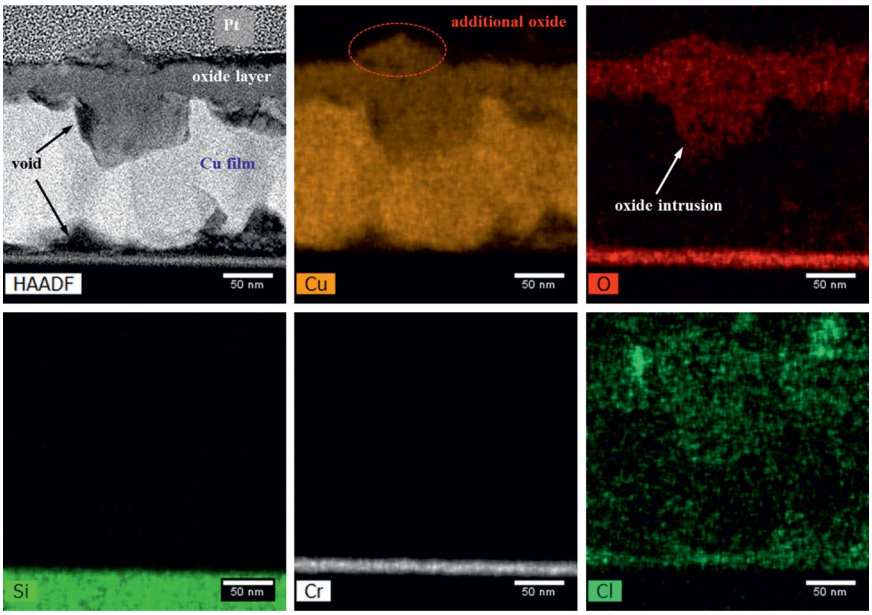

Figure 7. STEM HAADF cross-sectional image and EDX elemental maps showing exemplary the microstructure and spatial elemental distribution of Cu, O, Si, Cr and Cl after electrochemical treatment.

chemically grown oxide films, differences of structure observed in electrolyte and outside the electrolyte are frequently observed.[65]

A chemical analysis of the surface after the electrochemical treatment was performed by XPS, including depth profiling (Fig. 9). The oxidation state of the copper was determined in the Cu 2p spectra with the help of the satellite peaks. The surface spectrum of the layer

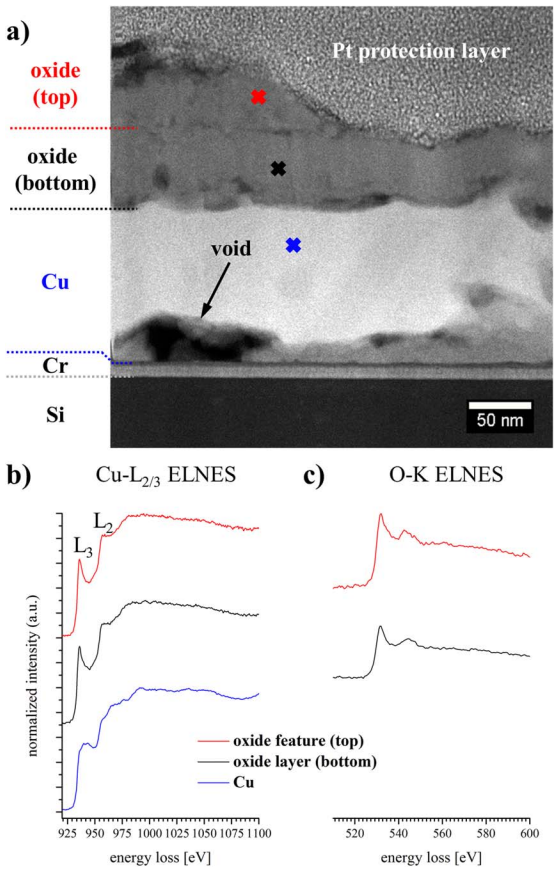

Figure 8. (a) STEM HAADF image showing exemplary the location where the presented EELS spectra were taken. (b) Cu $L_{2/3}$ and (c) O K near-edge fine structures of the upper oxide feature (red), the lower oxide layer (black) and the Cu thin film (blue).

from the CA experiment (Fig. 9a) shows a satellite peak in the Cu 2p region between 946 and 947 eV, pointing toward the presence of Cu^{I}. Cu^{I} presence is confirmed by the Cu LMM spectrum.[66,67] A single sputtering step of ≈3 nm shows Cu metal in Cu LMM spectrum, however Cu 2p still indicates the presence of Cu^{I}. Fig. 9c presents the chloride spectrum. The surface spectrum shows a Cl $2p_{3/2}$ peak, which decreased in intensity upon sputtering into the material. It is important to note that chloride is present, though not prominently, on the surface. Local STEM-EDX imaging (Fig. 7) also shows that the concentration of Cl decreases from the surface into the thin film. It is worth noting that XPS is not a trace analysis technique; it is likely that the concentration of Cl within the thin film, as probed after sputtering, is below the XPS detection limit. Both the Cu 2p as well as the Cl 2p spectra support the conclusions drawn from STEM-EDX data on a representative large sample area.

Differences have been observed between results obtained in situ, and ex situ surface characterization, which could originate, e.g., from drying or contact with air. Therefore, ex situ Raman spectra were recorded, to be able to compare the results directly to the in situ spectra discussed above. Fig. 10 shows the Raman spectra of the sample after removal from the electrolyte with two different excitation wavelengths. The first striking difference to the respective in situ spectra is the strong photoluminescence (PL) background in the ex situ measurements. PL with different intensities depending on the experiments peaks at ≈1.65 eV with under excitation at 2.41 eV. PL peaking at this energy has been used as evidence for an oxygen-poor metastable phase.[37] The peak photon energy is in between the photon energies of singly charged and doubly charged oxygen vacancies,[37] supporting the interpretation of an oxygen-deficient oxide as source of this PL. Moreover, Raman features of Cu_4O_3 and Cu_2O are observed (compare Table I) in Fig. 10. The existence of Cu_4O_3 and Cu_2O are in line with in situ observations at intermediate potentials. An interpretation of the peak at ≈300 cm^{-1} is difficult, because both $Cu^{II}Cl_4^{2-}$ and CuO have Raman features at this wavelength. Moreover, the feature at ≈300 cm^{-1} is observed ex situ only when the sample is excited with 2.41 eV, while it was also visible at the excitation with 1.96 eV in the in situ experiments.

Discussion of layer formation and dissolution mechanism.—The thermodynamics of the system under investigation is best analyzed in terms of Pourbaix style predominance pH diagrams. The Pourbaix diagram of copper in PBS solution was calculated at the fixed concentrations of Cl^- and total phosphate in solution as 140 mM and 10 mM, respectively, in line with used electrolyte concentrations.

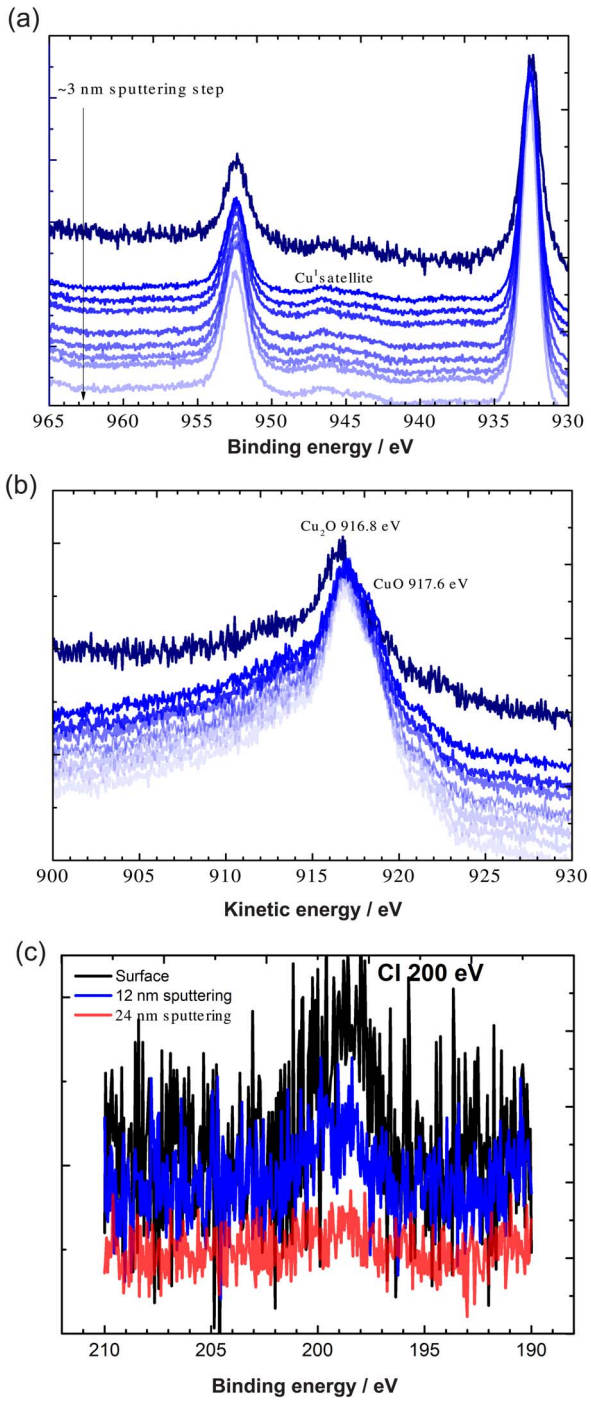

Figure 9. XPS sputter profiles of the layer after CA-SE experiments. The depth difference between the sputtering cycles was ≈3 nm. (a) Cu 2p spectra; (b) Auger Cu LMM spectra; (c) Cl 2p spectra.

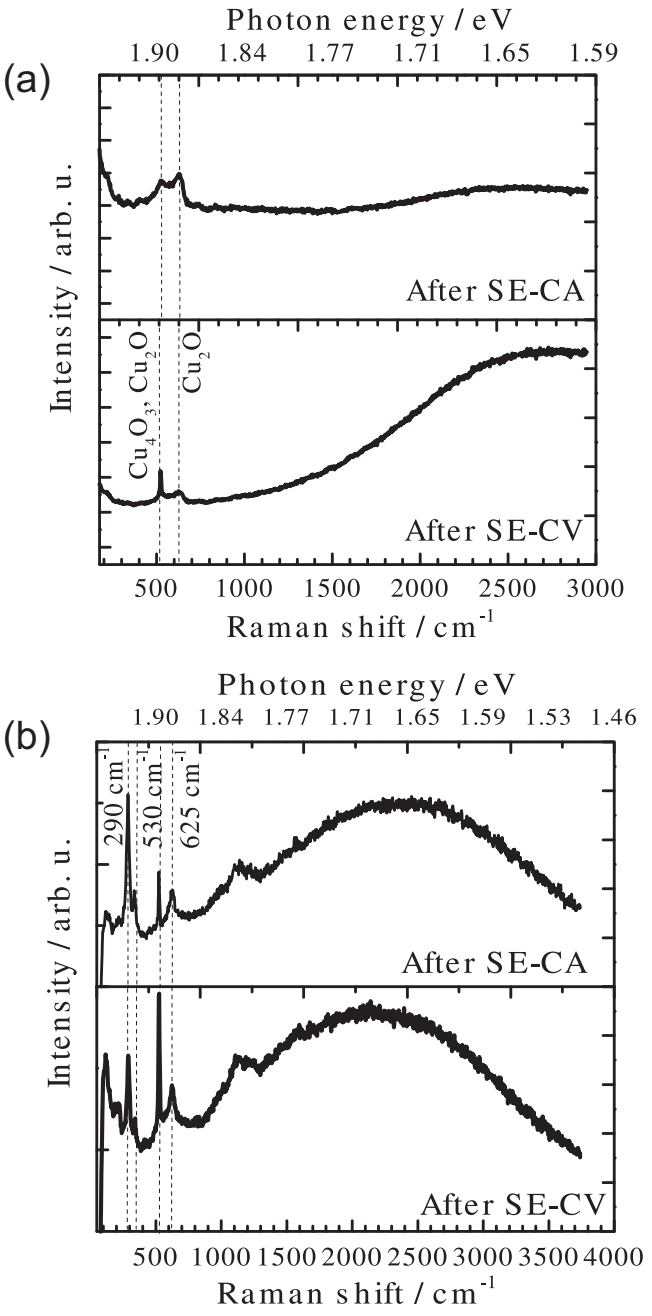

Figure 10. Ex situ Raman spectra after electrochemical in situ spectroscopic ellipsometry experiments, CA or CV as indicated in the graph; (a) excitation 633 nm/1.96 eV; (b) excitation 514 nm/2.41 eV. Numbers on the eV scale correspond to the closest second digit the wavelength of the respective Raman shift on the Raman shift axis.

Different scenarios regarding total copper concentration in solution were investigated, to map a wide range of experimental scenarios. Results for four copper ion concentrations are given in Fig. 11.

At the beginning of each experiment, the system should be in a regime of low copper ion concentration (Fig. 11a). This is also the situation when immersing the material first to a solution without copper, or bringing a solution with bacteria into contact with a copper surface. At pH 7 in the potential region between −1.2 V and 0.1 V, copper is supposed to be in the active state, and dissolves as

$$Cu + 2Cl^- \rightarrow Cu^{I}Cl_2^- + e^-. \quad [1]$$

At high electrode potentials, in the pH range between 5–7, formation of $Cu^{II}HPO_4$ is possible, but this phase was not observed in this work. In the course of an experiment, hydrogen may be evolved during cathodic polarization,

$$H_2O + e^- \rightarrow \frac{1}{2}H_2 + OH^-, \quad [2]$$

leading to a slow increase in pH. The increase is expected to be relatively mild in a phosphate buffered system, compared to unbuffered solutions.[68] Under anodic polarization, or under conditions of free corrosion, copper will slowly dissolve (Reaction 1), increasing the copper concentration, especially near the copper surface. Fig. 11 shows that CuCl precipitation is expected only at lower pH. At pH 7 and above,

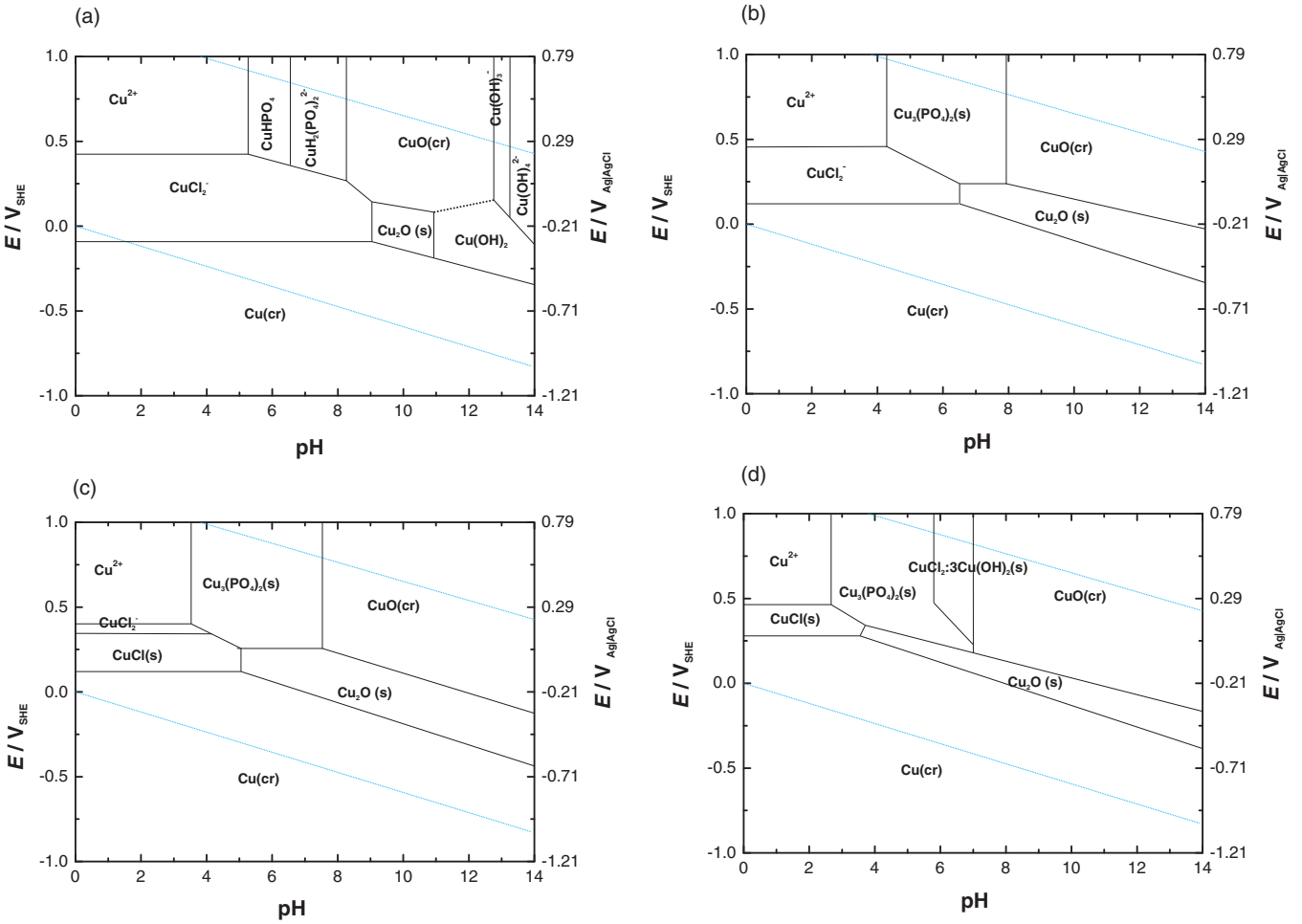

Figure 11. Predominance potential pH diagrams for copper in contact with PBS (140 mM Cl^-, 10 mM PO_4^{3-}) calculated using MEDUSA with the HYDRA database, for four different concentrations of total dissolved copper, including both Cu^+ and Cu^{2+}; (a) 10^{-6} M, (b) 1 mM, (c) 10 mM, (d) 1 M. The dotted line in (a) represents the ambiguous domain separation $Cu(OH)_2$ and CuO.

the system is supposed to be passive above copper ion concentrations of 1 mM, where Cu_2O should form at intermediate potentials, and different Cu^{II}-containing phases at higher potentials.[c]

The observation of Cu_2O in most of the experiments is hence expected after active dissolution of Cu which produced a sufficient amount of copper in solution. There is no fundamental difference here between the results from CA (Fig. 5) and CV (Fig. 2) experiments. In situ Raman spectra (Fig. 5c) do, however, show that Cu^I species are still present in the film in CA experiments at 0.1 V after long polarization times, while in CV experiments (Fig. 2b), they disappear. The different experiments are therefore discussed jointly. At higher potentials, no precipitation of phosphates was observed, as suggested by the predominance diagrams. Also, no passivation was observed. Most likely the equilibrium constant for the formation of the observed $CuCl_4^{2-}$,

$$Cu^{2+} + 4Cl^- \rightleftharpoons CuCl_4^{2-}, \quad [3]$$

which is included in the equilibrium constant K of the reaction

$$Cu^{+} + 4Cl^- \rightleftharpoons CuCl_4^{2-} + e^-, \quad [4]$$

given as $\log_{10} K = -6.5$ in HYDRA, is not accurate enough. The formation of a soluble Cu^{II} species, is, however, in agreement with the results from the surface analytical techniques.

In situ ellipsometry shows that in CA experiments at 0.1 V, a layer is present, which is also surprisingly stable in thickness, but does not lead to passivation. It must therefore be stable as a steady state layer. This layer must be rich in Cu^I. Ex situ analysis after the experiments show an incorporation of certain amounts of Cl^- into the layer. In situ experiments show also, via the presence of Cu_4O_3, the presence of a certain amount of Cu^{II}. The absorption spectra can be interpreted such that CuCl-like species are present, in agreement with the observations after in situ experiments. It is hence likely that the film dissolves as soon as species are oxidized to Cu^{II}, while it re-forms by oxidation of Cu to Cu^I.

The overall mechanism suggested based on the experimental results is summarized in Fig. 12. When polarizing from cathodic region positively, a Cu_2O film forms. This film is rich in point defects, as

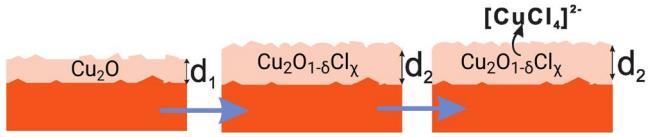

Figure 12. Schematic mechanism of film formation on copper and copper dissolution in PBS. On an initially oxide free surface, Cu_2O is forming at sufficiently high electrode potentials. Cl^- incorporates into the oxide layer, possibly by filling oxygen vacancies. As soon as the electrode potential is high enough to permit the oxidation to Cu^{II}, the film dissolves while $CuCl_4^{2-}$ becomes the dominating copper oxidation product.

[c] Cu_4O_3 is a metastable oxide, and as such not included in the Pourbaix diagram.

suggested by its absorption spectrum. Some of these are likely to be oxygen vacancies, in line with the ex situ PL observation. These can be compensated by uptake of Cl^-, resulting in the first step in a chloride-rich, copper(I) oxide based layer. As soon as the electrode potential increase triggers the oxidation from Cu^I to Cu^{II}, the formation of soluble $CuCl_4^{2-}$ sets in, which may have precursors inside the film, or adsorbed to the surface.

Summary and Conclusions

In situ spectroscopic investigation of the oxidation of copper in PBS electrolyte at pH 7 show that above a potential of ≈−0.05 V, a defect-rich Cu_2O formed. Formation of Cu_2O is in agreement with thermodynamic expectations based on the Pourbaix diagram of the system in the presence of chloride and phosphate. Upon further oxidation, a Raman signal started to dominate the spectra which has been assigned here as originating from square planar $CuCl_4^{2-}$. The fact that no passivation was observed is interpreted such that the $CuCl_4^{2-}$ species must have a significant solubility. Nevertheless, a layer with a thickness in the order of 10 nm was found at +0.1 V by spectroscopic ellipsometry, indicating that the continuing dissolution of copper proceeded via a layer of a steady state thickness. While in situ spectroscopy has shown signatures of the presence of Cu^{II} in form of Cu_4O_3, post mortem surface analysis confirmed only the dominance of Cu^I and traces of chloride. The lack of a dominating Cl^--containing species in post mortem surface analysis is in agreement with the interpretation of the presence of soluble $CuCl_4^{2-}$. However, Cl^- was detected along grain boundaries inside the copper. This ingress of chloride is likely to facilitate later dissolution under complex formation, and the formation of pits into the copper. No significant solid phases containing copper chlorides or copper phosphates have been detected. It is suggested that the dissolution of copper proceeds via chloride incorporation in oxygen vacancies in the defective Cu_2O. As dissolution in the presence of biological material often proceeds at near neutral pH in an environment containing significant amounts of Cl^-, the results obtained in this work may be relevant for the understanding of the surface electrochemistry of copper as antibacterial agent.

Acknowledgments

C.T. acknowledges the International Max Planck Research School for Surface and Interface Engineering in Advanced Materials (IMPRS SurMat) for a scholarship. A.A. and A.E. gratefully acknowledge the DFG (Deutsche Forschungsgemeinschaft) for the financial support of the subproject ER 601/3-2 within priority program 1640 “Joining by plastic deformation”. O.K. acknowledges a scholarship from the Alexander von Humboldt foundation. M. Stratmann is acknowledged for continuous support, and the MPIE workshop for building the in situ cells.

References

1. G. Grass, C. Rensing, and M. Solioz, *Appl. Environ. Microbiol.*, **77**(5), 1541 (2011).
2. F. Paladini, M. Pollini, A. Sannino, and L. Ambrosio, *Biomacromolecules*, **16**(7), 1873 (2015).
3. S. Medici, M. Peana, V. M. Nurchi, J. I. Lachowicz, G. Crisponi, and M. A. Zoroddu, *Coord. Chem. Rev.*, **284**, 329 (2015).
4. M. Hans, S. Mathews, F. Mücklich, and M. Solioz, *Biointerphases*, **11**(1), 018902 (2016).
5. A. M. Alfantazi, T. M. Ahmed, and D. Tromans, *Mater. Des.*, **30**(7), 2425 (2009).
6. M. M. Antonijević, S. M. Milić, and M. B. Petrović, *Corros. Sci.*, **51**(6), 1228 (2009).
7. G. S. Frankel, *J. Electrochem. Soc.*, **145**(6), 2186 (1998).
8. S. Bennici and A. Gervasini, *Appl. Catal., B*, **62**(3–4), 336 (2006).
9. S. Anandan, X. Wen, and S. Yang, *Mater. Chem. Phys.*, **93**(1), 35 (2005).
10. V. Brusic, M. A. Frisch, B. N. Eldridge, F. P. Novak, F. B. Kaufman, B. M. Rush, and G. S. Frankel, *J. Electrochem. Soc.*, **138**(8), 2253 (1991).
11. G. T. Burstein, H. Bi, and G. Kawaley, *Electrochim. Acta*, **191**, 247 (2016).
12. M. Hans, A. Erbe, S. Mathews, Y. Chen, M. Solioz, and F. Mücklich, *Langmuir*, **29**(52), 16160 (2013).
13. C. L. DuPont, G. Grass, and C. Rensing, *Metallomics*, **3**(11), 1109 (2011).
14. J. Kunze, V. Maurice, L. H. Klein, H.-H. Strehblow, and P. Marcus, *J. Phys. Chem. B*, **105**(19), 4263 (2001).
15. J. Kunze, V. Maurice, L. H. Klein, H.-H. Strehblow, and P. Marcus, *Electrochim. Acta*, **48**(9), 1157 (2003).
16. H.-H. Strehblow, V. Maurice, and P. Marcus, *Electrochim. Acta*, **46**(24-25), 3755 (2001).
17. C. Toparli, A. Sarfraz, and A. Erbe, *Phys. Chem. Chem. Phys.*, **17**(47), 31670 (2015).
18. H. Y. H. Chan, C. G. Takoudis, and M. J. Weaver, *J. Phys. Chem. B*, **103**(2), 357 (1999).
19. C. Molteni, H. K. Abicht, and M. Solioz, *Appl. Environ. Microbiol.*, **76**(12), 4099 (2010).
20. D. L. Cocke, G. K. Chuah, N. Kruse, and J. H. Block, *Appl. Surf. Sci.*, **84**(2), 153 (1995).
21. I. Platzman, R. Brener, H. Haick, and R. Tannenbaum, *J. Phys. Chem. C*, **112**(4), 1101 (2008).
22. C. Gattinoni and A. Michaelides, *Surf. Sci. Rep.*, **70**(3), 424 (2015).
23. M. R. G. de Chialvo, R. C. Salvarezza, D. Vasquez Moll, and A. J. Arvia, *Electrochim. Acta*, **30**(11), 1501 (1985).
24. E. Huttunen-Saarivirta, P. Rajala, and L. Carpén, *Electrochim. Acta*, **203**, 350 (2016).
25. G. Mankowski, J. P. Duthil, and A. Giusti, *Corros. Sci.*, **39**(1), 27 (1997).
26. P. Marcus, V. Maurice, and H. H. Strehblow, *Corros. Sci.*, **50**(9), 2698 (2008).
27. G. S. Frankel and N. Sridhar, *Mater. Today*, **11**(10), 38 (2008).
28. A. Nishikata, M. Itagaki, T. Tsuru, and S. Haruyama, *Corros. Sci.*, **31**, 287 (1990).
29. B. Jeon, S. K. R. S. Sankaranarayanan, A. C. T. van Duin, and S. Ramanathan, *ACS Appl. Mater. Interfaces*, **4**(3), 1225 (2012).
30. G. Kear, B. D. Barker, and F. C. Walsh, *Corros. Sci.*, **46**(1), 109 (2004).
31. H. P. Lee and K. Nobe, *J. Electrochem. Soc.*, **133**(10), 2035 (1986).
32. G. Bianchi, G. Fiori, P. Longhi, and F. Mazza, *Corrosion* (Houston, TX, U. S.), **34**(11), 396 (1978).
33. M. Braun and K. Nobe, *J. Electrochem. Soc.*, **126**(10), 1666 (1979).
34. G. Faita, G. Fiori, and D. Salvadore, *Corros. Sci.*, **15**(6), 383 (1975).
35. J. C. Hamilton, J. C. Farmer, and R. J. Anderson, *J. Electrochem. Soc.*, **133**(4), 739 (1986).
36. L. Debbichi, M. C. Marco de Lucas, J. F. Pierson, and P. Krüger, *J. Phys. Chem. C*, **116**(18), 10232 (2012).
37. B. K. Meyer, A. Polity, D. Reppin, M. Becker, P. Hering, P. J. Klar, T. Sander, C. Reindl, J. Benz, M. Eickhoff, C. Heiliger, M. Heinemann, J. Bläsing, A. Krost, S. Shokovets, C. Müller, and C. Ronning, *Phys. Status Solidi B*, **249**, 1487 (2012).
38. H. H. Strehblow and B. Titze, *Electrochim. Acta*, **25**(6), 839 (1980).
39. G. Barati, V. Solokha, K. Wandelt, K. Hingerl, and C. Cobet, *Langmuir*, **30**(48), 14486 (2014).
40. Y. Chen, P. Schneider, and A. Erbe, *Phys. Status Solidi A*, **209**(5), 846 (2012).
41. Y. Chen and A. Erbe, *Surf. Sci.*, **607**, 39 (2013).
42. G. Genchev and A. Erbe, *J. Electrochem. Soc.*, **163**(6), C333 (2016).
43. L. A. Giannuzzi and F. A. Stevie, *Micron*, **30**(3), 197 (1999).
44. R. M. Langford, *Microsc. Res. Tech.*, **69**(7), 538 (2006).
45. R. M. Langford and M. Rogers, *Micron*, **39**(8), 1325 (2008).
46. C. C. Ahn, *Transmission Electron Energy Loss Spectrometry in Materials Science and the EELS Atlas*. Wiley-VCH, Weinheim, Germany, 2nd ed. (2004).
47. R. F. Egerton, *Electron Energy-Loss Spectroscopy in the Electron Microscope*. Springer, New York, U.S., 3rd ed. (2011).
48. J. Scott, P. J. Thomas, M. MacKenzie, S. McFadzean, J. Wilbrink, A. J. Craven, and W. A. P. Nicholson, *Ultramicroscopy*, **108**(12), 1586 (2008).
49. V. Maurice, H.-H. Strehblow, and P. Marcus, *J. Electrochem. Soc.*, **146**(2), 524 (1999).
50. V. Maurice, H. H. Strehblow, and P. Marcus, *Surf. Sci.*, **458**(1–3), 185 (2000).
51. D. Tromans and R.-h. Sun, *J. Electrochem. Soc.*, **138**(11), 3235 (1991).
52. R. L. Frost, P. A. Williams, W. Martens, J. T. Kloprogge, and P. Leverett, *J. Raman Spectrosc.*, **33**(4), 260 (2002).
53. C. Toparli, A. Sarfraz, A. D. Wieck, M. Rohwerder, and A. Erbe, *Electrochim. Acta*, **236**, 104 (2017).
54. K. Eltsov, G. Zueva, A. Klimov, V. Martynov, and A. Prokhorov, *Chem. Phys. Lett.*, **158**(3), 271 (1989).
55. G. Niaura and A. Malinauskas, *Chem. Phys. Lett.*, **207**(4), 455 (1993).
56. G. Brown and G. Hope, *J. Electroanal. Chem.*, **405**(1-2), 211 (1996).
57. M. A. Nusimovici and A. Meskaoui, *Phys. Status Solidi B*, **52**(2), K69 (1972).
58. B. Prevot and M. Sieskind, *Phys. Status Solidi B*, **59**(1), 133 (1973).
59. I. P. Kaminow and E. H. Turner, *Phys. Rev. B*, **5**, 1564 (1972).
60. I. R. Beattie, T. R. Gilson, and G. A. Ozin, *J. Chem. Soc. A*, 534 (1969).
61. N. J. Doran and A. M. Woolley, *J. Phys. C: Solid State Phys.*, **12**(8), L321 (1979).
62. C. Scheu, G. Dehm, M. Rühle, and R. Brydson, *Philos. Mag. A*, **78**(2), 439 (1998).
63. R. D. Leapman, L. A. Grunes, and P. L. Fejes, *Phys. Rev. B*, **26**(2), 614 (1982).
64. F. Hofer and P. Golob, *Ultramicroscopy*, **21**(4), 379 (1987).
65. I. Díez-Pérez, F. Sanz, and P. Gorostiza, *Curr. Opin. Solid State Mater. Sci.*, **10**(3–4), 144 (2006).
66. G. Panzner, B. Egert, and H. Schmidt, *Surf. Sci.*, **151**, 400 (1985).
67. K. J. Blobaum, D. Van Heerden, A. J. Wagner, D. H. Fairbrother, and T. P. Weihs, *J. Mater. Res.*, **18**, 1535 (2003).
68. M. Auinger, I. Katsounaros, J. C. Meier, S. O. Klemm, P. U. Biedermann, A. A. Topalov, M. Rohwerder, and K. J. J. Mayrhofer, *Phys. Chem. Chem. Phys.*, **13**, 16384 (2011).
69. R. L. Frost, W. Martens, J. T. Kloprogge, and P. A. Williams, *J. Raman Spectrosc.*, **33**(10), 801 (2002).